RSC Advances

RSC Advances

www.rsc.org/advances

ROYAL SOCIETY OF CHEMISTRY

www.rsc.org/advances

Journal Name

RSC Advances

Dynamic Article Links ▶

ARTICLE TYPE

Ti₅Si₃/β-Ti nano-core-shell structure toughened glassy Ti alloy matrix biocomposites

Chunxiang. Cui,* Ling Bai, Shuangjin Liu, Yumin Qi and Lichen Zhao

In the experiment, the Ti75Zr11Si9Fe5 and Ti66Zr11Si15Fe5Mo3 ingots were prepared by vacuum arc-melting furnace. Both Ti alloy ribbons of 3-5mm in width and about 80 um in thickness were made into from bulk samples by an as-quenched technique under an argon atmosphere. Both melt-spun glassy ribbons exhibit large supercooled liquid regions, high reduced glass transition temperatures, and good 10 thermal stabilities. For both alloys, the stable phases after heating are Ti glassy matrix and *in situ* nano-Ti₅Si₃ particles encircled by nano shell of β-Ti. After the Ti₅Si₃/β-Ti nano-core-shell structure was *in situ* formed, *in situ* Ti₅Si₃/β-Ti nano-core-shell structure toughened glassy Ti alloy matrix composites were prepared. For the Ti66Zr11Si15Fe5Mo3 ribbons, its high strength is attributed to both Mo solution strengthening and nano core-shell Ti₅Si₃/β-Ti toughening and dispersion strengthening. Observations and 15 analysis on microstructure and fracture morphology of melt-spun glassy ribbons indicated that multi-slip bands were formed during the tensile test.

1. Introduction

The Ti-based alloys are widely used as traditional structural and engineering materials because of their excellent corrosion 20 behavior, low density, and attractive fracture related properties. The extensive applications in aviation industry stimulate the development of light Ti alloys with optimized mechanical property combinations. For cast Ti alloys, the room temperature tensile strength is in the range 700–1150 MPa together with 25 elongations of 7–12% [1]. For cast and wrought Ti alloys subjected to aging, the typical ultimate tensile strength reaches 900–1500 MPa as well as elongations of 5–25%[2]. In addition, a number of studies on amorphization of Ti-based alloys have been carried out for the last two decades presumably because the 30 amorphization is expected to cause remarkable increases in mechanical strength, ductility and corrosion resistance. As a result, Ti-rich bulk glassy alloys have been found in rapidly solidified Ti-Cu-Al [1], Ti-Cu-Ni (Co) [2], Ti-Cu-Zr-Ni [3], Ti-Cu-Co-Al-Zr [4] and Ti-Cu-Ni-Sn (Si) [5] systems to date. Since 1988, 35 a number of alloys[6] with a high glass-forming ability and able to be fabricated as bulk metallic glasses (BMGs) have been discovered in multicomponent Mg, La, Zr, Fe, and Pd-based, alloy systems. Recently, the Ti-base bulk metallic glasses (BMGs) developed exhibit a tensile strength of up to 2000 MPa [6]. 40 However, the BMGs usually show very small plasticity due to the formation of highly localized shear bands under loading [7]. The localized shear bands lead to 'work-softening', resulting in catastrophic fracture with insignificant strain [7-9]. Many attempts have been devoted to reinforce BMGs, either by particle 45 reinforcement [10–12], fiber-reinforcement [13-16] or *in situ* formation of ductile bcc-phase precipitates [17-19]. Zhu SL et. al. investigated the effects of small amounts of Si on the glass-forming ability, thermal stability and mechanical property of a TiZrCuPdSn bulk metallic glass[20]. Zhu indicated that the

50 addition of Si caused the decrease of glass-forming ability and the enlarging of the supercooled liquid (SCL) region. With 2 at.% Si addition, a significant SCL region of 80 K was obtained, which indicated high thermal stability of the glassy alloy and was in favor of secondary working by viscous flow deformation. With 55 increasing Si content, the plasticity decreased. [20]. Yin and Zhu so far revealed the effects of small amounts of Si on the fragility, crystallization behaviors and the glass transition of a Ti40Zr10Cu36Pd14Si bulk glassy alloy. They indicated that the fragility of the alloys containing Si was higher than that of the Si-60 free alloy [20,21,22]. In the glass transition process, both generation and annihilation of free volumes are suppressed by the addition of 1-3 at% Si, and excess Si could make Si rich regions formed in the amorphous titanium alloy matrix [21, 23]. Recent research shows that Si element can obviously increase the solid solution 65 strengthening effect and the amorphous formation ability of Ti-Ni-Si and Ti-Zr-Si alloys [24, 25].

Pang et al. studied the corrosion behavior of a glassy Ti-Zr-Hf-Cu-Ni-Si alloy, and they indicated that there were the lower corrosion rates for the glassy Ti41.5Zr2.5.Hf5Cu42.5Ni7.5Si1 by 70 the addition of 1 at% Si, alloy in the solutions [26].

Li and He investigated the effects of Mo on the glass-forming ability and crystallization behavior of Ti-Cu-Ni-Sn-Mo bulk metallic glass [27, 28]. They found that the Mo addition decreased the glassy phase content and also refined the microstructure of the 75 alloy layer, leading to the improvement of the wear resistance [27,28].

We have extensively investigated Ti-base BMGs with the aim to improve their plasticity. Since the glass-forming ability for Ti-base BMGs is not as high as for Zr-base BMGs, it is difficult to 80 cast large size bars or rods (e.g. with a diameter larger than 5 mm) with fully glassy structure.

We have selected one of the bio-Ti-base BMGs with the largest glass-forming ability and no biological toxicity characteristics,

Ti70Zr12Fe8Si10, and modified the alloy by addition of various contents of Mo and Si. Up to 5% plastic strain together with an ultimate compressive strength of 2085 MPa at room temperature can be achieved for both Ti75Zr11Si9Fe5 (At %) and Ti66Zr11Si15Fe5Mo3 (At %) melt-spun glassy ribbons. ons.

In this paper, we present results for reinforced Ti-base BMG-forming alloys that contain no biotoxic elements. The microstructure, the thermal stability, the phase transformation behavior, amorphous formation ability, the tensile deformation characteristics and fracture morphology are investigated. So we hope that these alloys could be developed into a new type of titanium matrix composites with good plasticity, high strength, excellent corrosion resistance and biocompatibility.

2. Metals and Methods

In the experiment, the buttony Ti-based alloy ingots, both Ti75Zr11Si9Fe5 (At %) and Ti66Zr11Si15Fe5Mo3 (At %), were prepared by arc-melting a mixture of pure (≥99.8) Ti, Zr, Fe, Si and Mo metals respectively in a purified argon atmosphere. Alloy ribbons of 3-5mm in width and about 80 um in thickness were made into from bulk samples by an as-quenched technique under an argon atmosphere. The circumferential velocities of the-molybdenum wheel were 50m/s. The oxygen content of the as-cast cylinders was chemically analyzed to be less than 200 ppm. All the ribbons were studied by differential scanning calorimetry (DSC) by both constant-rate heating as well as by isothermal annealing in a flowing argon atmosphere using a Perkin–Elmer DSC 7 calorimeter. Scanning electron microscopy (SEM) (JEOL4800 microscope) was used for the analysis of the ribbons' morphologies and for characterization of fracture features. The phase compositions and the microstructures were investigated using a Philips X'Perd BMP X-ray diffractometer with CuKα□radiation and FEI Tacnai F20 high resolution transition electron microscopy (HRTEM). The samples for the tensile tests were prepared according to ASTM standards. The compression properties were tested by using an MTS 810 testing machine at a strain rate of 0.02 m / s at room temperature.

3. Results and discussion

In this paper, the glass-forming ability (GFA) of the both alloys is investigated according to Inoue's three empirical rules and supercooled liquid region before crystallization, respectively. Most reported bulk glassy alloys except Pd-based alloys have those simple empirical component rules. Inoue generalized the three empirical rules [8] by taking into account important quantities, such as amount of alloy element, significantly different atomic size ratios, and mixing among the constituent elements. Firstly, both Ti75Zr11Si9Fe5 (At %) and Ti66Zr11Si15Fe5Mo3 (At %) consist of more than three elements. Moreover, as Ti66Zr11Si15Fe5Mo3 (At %) alloy, the addition of Mo is effective for increasing in the degree of the satisfaction of the three empirical rules, which may to some extent account for the reason why the alloy Ti66Zr11Si15Fe5Mo3 (At %) is superior to another alloy in amorphous phase forming ability.   Secondly, significantly different atomic size ratios are above about 12% among the constituent elements. The rearrangement of the constituent elements with different atomic sizes may lead to a higher packing

density. The atomic size of an element is quoted from a data book [9] as the atomic radius which is taken as half of the interatomic distance in a crystalline state. Based on the data for the atomic radius of elements, the atomic sizes of both alloys change more continuously in the order of Zr > Ti > Fe >> Si. Finally, the both alloys process negative heats of mixing among the elements. The generation of atomic pairs with various negative heats of mixing also increases the thermal stability of the supercooled liquid since a large amount of active energy is required for crystallization. Furthermore, for amorphous alloy Ti66Zr11Si15Fe5Mo3 (At %), the addition of Mo effectively increases the numbers of atomic pairs with negative heats of mixing, such as Ti-Mo as well as Si-Mo. The values of heat of mixing were quoted as enthalpy of mixing (ΔH_{AB}^{mix}) [10] of the binary liquid in an A-B systems at an equi-atomic composition. Table 1 [8] shows the values of ΔH_{AB}^{mix} (KJ/mol) calculated by Miedema's model for atomic pairs between elements in the both alloys. The mixing enthalpy of solid solution is comprised of chemical, elastic, and structural terms [11]. Since elastic, and structural contributions are absent in the liquid, the mixing enthalpy consists of only the chemical term, which can be determined by the regular melt model[11,12],

$$\Delta H^{mix} = \sum_{i=1,i\neq j}^{n} \Omega_{ij} c_i c_j$$

Where ($\Omega_{ij} = 4 \Delta H_{AB}^{mix}$) is the regular melt interaction parameter between ith and jth elements, c_i is the atomic percentage of the ith component, and ΔH_{AB}^{mix} is the mixing enthalpy of binary liquid alloys. The calibration value of ΔH_{AB}^{mix} is used as

$$\Delta H_{AB}^{mix\,(cali)} = \Delta H_{AB}^{mix} - \Delta H^{trans} / 2$$

for containing one nontransition metal and

$$\Delta H_{AB}^{mix\,(cali)} = (\Delta H_i^{trans} + \Delta H_j^{trans}) / 2$$

for containing two nontransition metals. ΔH^{trans} can be 100, 30, 180, 310, 17, 34, and 25KJ mol-1 , respectively, for containing H, B, C, N, Si, P, and Ge [11]. According to the data mentioned above, the enthalpies of mixing of the both alloys are −159.348 KJ/mol and -117.8748 KJ/mol, respectively. It is noted that the former is more negative in comparison with the latter, which also explains to some extent why the amorphous forming ability of Ti66Zr11Si15Fe5Mo3 (At %) is superior to that of the other alloy.
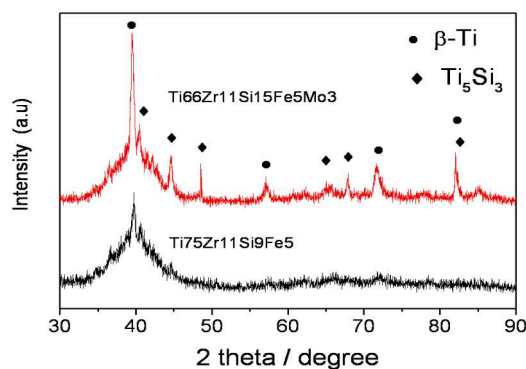
Figure 1. X-ray diffraction patterns of the as-quenched

Ti75Zr11Si9Fe5 (At %) and Ti66Zr11Si15Fe5Mo3 (At %).

Multi-component alloys system, different atomic size ratios above 12% and negative heats of mixing may lead to the formation of a highly dense random packed structure with low
5 atomic diffusivity. It is generally believed that the higher the packing density, the higher the thermal stability and the higher the resistance of the supercooled liquid against transformation into crystalline phase [13].

Amorphous structure of the melt-spun for Ti75Zr11Si9Fe5 and
10 glassy and nanocrystal structure for Ti66Zr11Si15Fe5Mo3 were confirmed by the XRD patterns, as shown in Figure 1. A broad peak arising from an amorphous phase can be seen in the 2θ range from 32 to 50º (Figure 1), which suggests that the both alloys all have excellent amorphous-forming ability. However, it
15 is obvious that the alloy Ti75Zr11Si9Fe5 is superior to another alloy in glass-forming ability. The reason why the alloys can have high glass-forming ability (GFA) through the stabilization of supercooled liquid region has been attributed to the formation of a novel glassy structure which is characterized by highly dense
20 packing, new local atomic configuration and long-range homogeneity with attractive interaction [7].
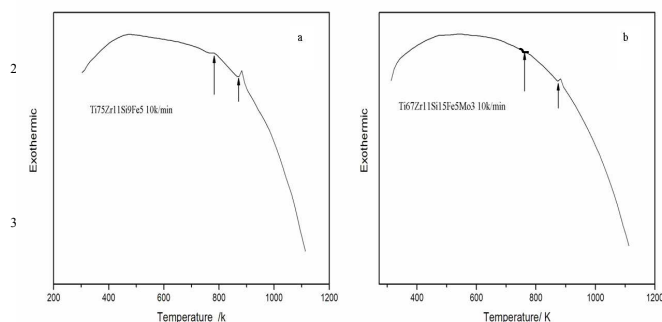
35 Figure 2. Differential scanning calorimetric (DSC) curves of amorphous both Ti75Zr11Si9Fe5 (At %) and Ti66Zr11Si15Fe5Mo3 (At %).

Differential scanning calorimetric (DSC) curves of both
40 Ti75Zr11Si9Fe5 and Ti66Zr11Si15Fe5Mo3 amorphous alloys is shown in Figure 2. A distinct and wide glass transition region can be found in Figure 2. Both Ti75Zr11Si9Fe5 and Ti66Zr11Si15Fe5Mo3 melt-spun glassy ribbons exhibit two exothermic peaks around 780–860 and 777–867 K, respectively,
45 as shown in Figure 2a and 2b. The supercooled liquid region (ΔT_x) before crystallization of the both alloys is about 80 K and 90 K, respectively, which is unusual in Ti-based amorphous alloy system. The single exothermic peak results from the simultaneous precipitation of several kinds of crystalline phases. The
50 crystalline mode implies that the atomic rearrangements of the constituent elements on a long-range scale are necessary for the progress of the crystallization reaction. The necessity causes the retardation of crystallization reaction which leads to the high thermal stability of the supercooled liquid. In the large
55 supercooled liquid, the topological and chemical short-range orderings are enhanced, leading to the formation of a highly dense random packed structure with low atomic diffusivity. It is generally believed that the higher the packing density, the higher

the thermal stability and the higher the resistance of the
60 supercooled liquid against transformation into crystalline phase [12]. All these further improve the glass-forming ability of Ti75Zr11Si9Fe5 and Ti66Zr11Si15Fe5Mo3 alloy ribbons. Therefore, it can be consolidated into a bulk form by utilizing the large viscous flow in the supercooled liquid region. Figure 2
65 shows the isothermal DSC traces recorded at different annealing temperatures for both alloys. Integrating the exothermic peaks allows obtaining the enthalpies of the phase transformation. The isothermal DSC data indicated that Mo increases the thermal stability of the supercooled liquid.
70 The corresponding TEM images, selected area electron diffraction (SAED) patterns and SAED analysis for the two kinds of ribbon samples are shown in Figure 3. As can be seen, Figure 3a shows that microstructures of the Ti75Zr11Si9Fe5 ribbon mainly consist of the grey continuous amorphous phase matrix
75 and a small amount of dark silica-rich nano-zones, so nearly all the structures are glassy state. Figure 3b shows that there are amorphous diffraction halo and some faint diffraction spots, which is consistent with the XRD pattern of the Ti75Zr11Si9Fe5 ribbons in Figure 1. As shown in Figure 3b, the diffraction halo
80 indicates that the matrix phase of the Ti75Zr11Si9Fe5 ribbon is amorphous, and some faint diffraction spots indicates that a small amount of dark zones are the Si rich regions, no obviours cystiform β-Ti phase with a shell structure is observed. As shown in Figure 3c, microstructures of the Ti66Zr11Si15Fe5Mo3 ribbon
85 consist of the grey continuous amorphous phase matrix and dark nanoparticles coated with bright nano-shell of β-Ti. Figure 3c shows that the sizes of $in\ situ$ Ti_5Si_3 nanoparticles encircled by β-Ti core-shell structure recognized as reinforcing phase are estimated in the range of 10.4-26.9 nm in diameter. What is more,
90 the nano-particles with the core-shell structure are distributed uniformly in the amorphous phase matrix. By means of TEM observation, we can find that each core-shell in the Ti66Zr11Si15Fe5Mo3 ribbon is a very thin cystiform β-Ti layer shell formed around the dark Ti_5Si_3 nano-particles, as shown in
95 the TEM images of Figure 3c. Figure 3d shows the SAED in the selected area of Figure 3c. From the SAED in figure 3d, we can find that it is composed of polycrystalline diffraction rings of nano core-shell structure and diffraction halo of amorphous matrix for the Ti66Zr11Si15Fe5Mo3 ribbons. Therefore, it is
100 obvious that SAED results in Figure 3d are consistent with the XRD pattern of the Ti66Zr11Si15Fe5Mo3 ribbons in Figure 1. So the SAED does show spots attributed to the Ti5Si3/beta-Ti nanoparticles and amorphous ring likely attributed to the surrounding amorphous matrix. Figure 3e shows TEM image of
105 Ti_5Si_3/β-Ti core-shell structure for Zone A in Figure 3c. Based on the SAED analysis on the zone "A" in the Figure 3c, Figure 3f shows that there are β-Ti phase and Ti_5Si_3 phase in this area. It is indicated by HREM observation that Ti_5Si_3/β-Ti interface possess core-shell microstructure, $d(210)_{Ti5Si3} = 0.24419$ nm, and $d(110)_{\beta\text{-}Ti} = 0.2337$ nm, and the difference between both lattice spacing is
110 $_{Ti} = 0.2337$ nm, and the difference between both lattice spacing is very little, so β-Ti crystal grow with (110) plane around the (210) plane of Ti_5Si_3 nanocrystals, as shown in Figure 3g. Figure 3h shows the schematic diagram of Ti_5Si_3/β-Ti core-shell distributed in glassy Ti alloy matrix.
115 As we know, almost all of the amorphous metals possess very excellent mechanical properties, but poor toughness. If we want to improve the toughness of amorphous metals, the use of nanocrystalline particles toughened amorphous matrix is theoretically one good way. Therefore, to study the formation
120 mechanism of nano-shell structure in the amorphous alloy matrix is very necessary.
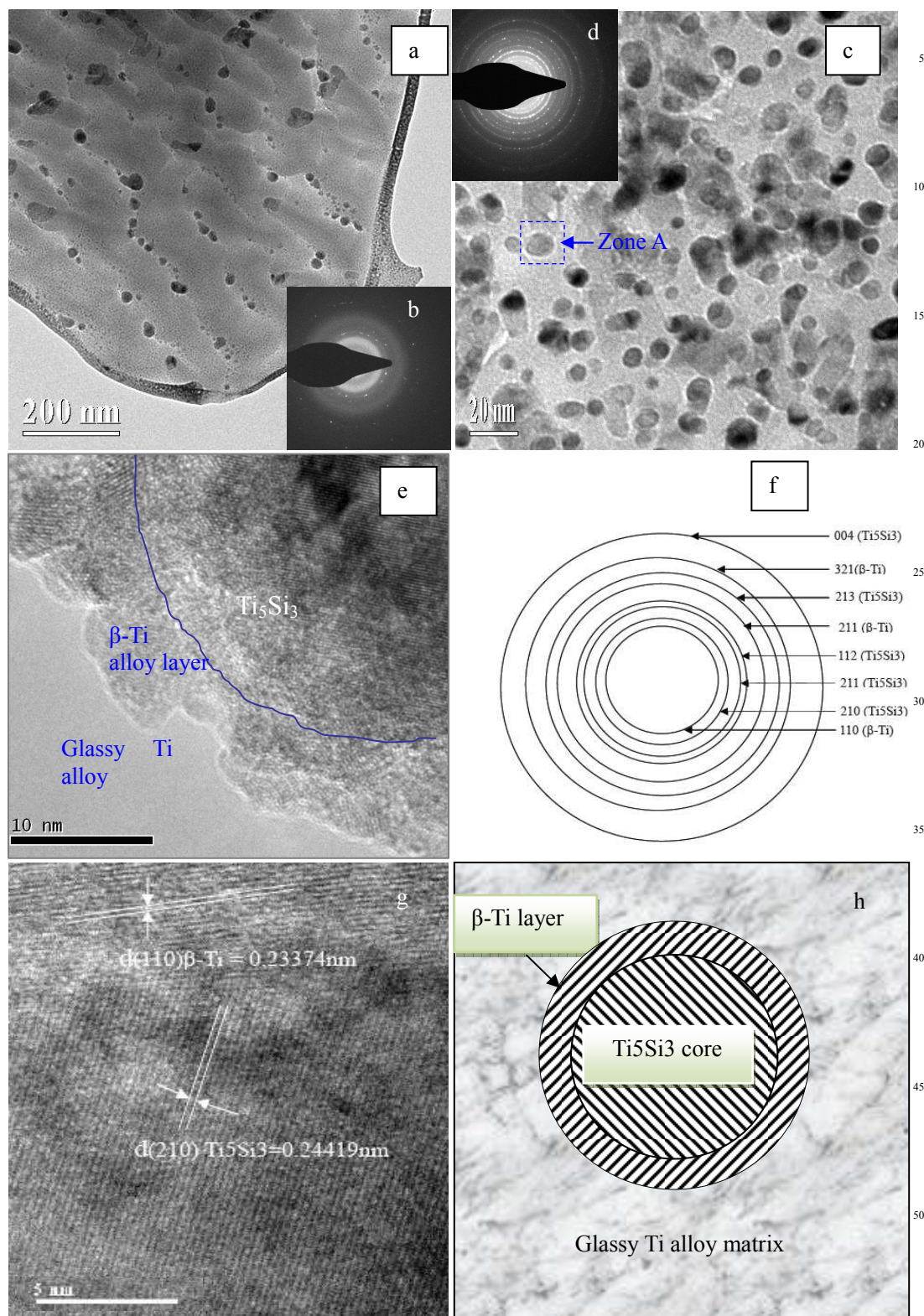
Figure 3. TEM images and SEAD analysis of the glassy Ti alloy ribbons. (a) TEM image of the Ti75Zr11Si9Fe5 ribbon (b) SEAD in the selected area of Figure 3a (c) TEM images of the Ti66Zr11Si15Fe5Mo3 ribbon (d) SEAD in the selected area of Figure 3c (e) TEM image of Ti_5Si_3/β-Ti core-shell structure for Zone A in Figure 3c (f) the corresponding SEAD analysis for polycrystalline diffraction rings in Figure 3d (g) HREM image of Ti_5Si_3/β-Ti core-shell interface microstructure (h) schematic diagram of Ti_5Si_3/β-Ti core-shell distributed in glassy Ti alloy.
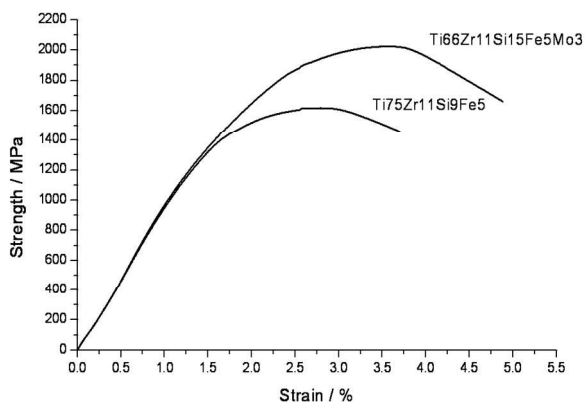
Figure 4. Room temperature tensile stress–strain curves of (a) Ti66Zr11Si15Fe5Mo3 (At %) and (b) Ti75Zr11Si9Fe5 (At %) alloy ribbons.

5
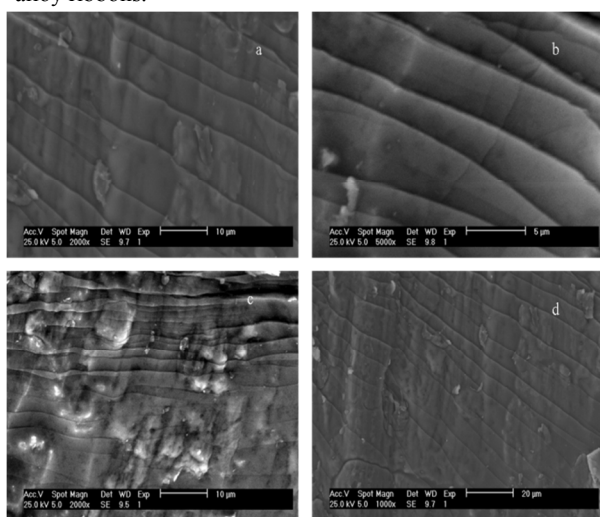
Figure 5. Fracture surfaces of two kinds of bio Ti base alloy ribbons after tensile testing: (a) formation of slip band patterns on the surface of Ti66Zr11Si15Fe5Mo3 (At %)
1 sample during the yield deformation; (b) micro-appearance of the shear band array with protuberance on the fracture surface of the specimen of Ti66Zr11Si15Fe5Mo3 (At %); (c) formation of slip band patterns on the fracture surface of Ti75Zr11Si9Fe5 alloy ribbons during the yield deformation:
1 shear slip bands with protuberance, and (d) fracture of shear bands over the entire fracture surface of Ti75Zr11Si9Fe5 alloy ribbons after tensile testing.

According to the Ti-Si binary alloy phase diagram, when the
20 atom content of Si is more than 10%, at the melting temperature of the Ti-15Si alloy, the Ti alloy enters into solid-liquid dual phase region (L+ Ti$_5$Si$_3$). Since the melting point of 2130 ℃ for the Ti$_5$Si$_3$ phase is much higher than the melting point of the matrix alloy, Ti$_5$Si$_3$ phase has become the nano-solid particles
25 distributed with a suspended state in the titanium alloy melt. When Ti alloy is solidificated rapidly, Ti$_5$Si$_3$ nanoparticle phase becomes the heterogeneous nucleation in the Ti alloy melt. However, amorphous alloy forming ability of Ti66Zr11Si15Fe5Mo3 is so strong that Ti$_5$Si$_3$ phase nanoparticles
30 only put around their surroundings of melt to form a thin

crystalline layer of Ti alloy. Statements as above are the formation mechanism of Ti$_5$Si$_3$/β-Ti nano core-shell structure in the glassy Ti alloy matrix for Ti66Zr11Si15Fe5Mo3.

Actually, even though some small *in situ* nanoparticles coated
35 crystal shell structure are also visible during the HRTEM observation, their size and volume fraction are too small to be detected very clearly by XRD patterns, but SAED analysis indicates that they are Ti$_5$Si$_3$ phase and β-Ti phase, as shown in Figure 3f. In situ Ti$_5$Si$_3$ nanoparticles coated β-Ti core-shell
40 structure can be homogeneously distributed in the amorphous Ti alloy matrix, which can be illustrated by Figure 3e. So, *in situ* Ti$_5$Si$_3$ nanoparticles coated β-Ti core-shell reinforced and toughened bio-Ti-base metallic glass matrix composite is fabricated out.
45

Table 1. The values of ΔH_{AB}^{mix} /KJ/mol calculated by Miedema's model for atomic pairs between elements.

	Ti	Zr	Fe	Si	Mo
Ti	0	0	-17	-66	**-4**
Zr	0	0	-25	-84	**-6**
Fe	-17	-25	0	-35	**-2**
Si	-66	-84	-35	0	**-35**
Mo	**-4**	**-6**	**-2**	**-35**	**0**

50 A series of tensile tests have been carried out for Ti75Zr11Si9Fe5 and Ti66Zr11Si15Fe5Mo3 alloy ribbons. Figure 4 shows typical room temperature tensile stress–strain curves. For the alloy Ti75Zr11Si9Fe5, the ultimate tensile stress reaches 1608 MPa with 3.71% plastic strain, yielding occurs at 1400 MPa, and
55 1.26% elastic strain is observed before yielding. For the alloy Ti66Zr11Si15Fe5Mo3 alloy ribbons, the ultimate tensile stress reaches 2085 MPa with 4.87% plastic strain, and yielding occurs at 1790 MPa, and 1.67% elastic strain is observed before yielding. The Young's modulus of both alloys is 94.3 GPa which is lower
60 than that of monolithic Ti-base BMGs (about 100 GPa) [12] and crystalline Ti alloys (about 120 GPa) [13]. Apparently, for the present alloy, the combination of strength and plasticity is superior to other Ti-base BMGs, Ti-base composites or Ti-Al-base intermetallics [14–20]. Based on the test data as above, we can
65 know as follows: For the Ti66Zr11Si15Fe5Mo3 ribbons, the main reasons for strengthening are both nano-core-shell structure and Mo solution in Ti alloy matrix; the toughening contribution comes mainly from the nano core-shell Ti$_5$Si$_3$/β-Ti. The Mo atoms promote the generation of *in situ* Ti$_5$Si$_3$ phase in the
70 Ti66Zr11Si15Fe5Mo3 ribbons.

For the Ti75Zr11Si9Fe5 alloy ribbons, some similar slip bands during the yield and deformation features on the fracture surface are observed, such as the formation of vein patterns along the shear-off direction (Figure 5a). Besides, a brittle feature of slip
75 bands deformed on the fracture surface is also observed (Figure 5b).

During the yield deformation process of Ti75Zr11Si9Fe5 alloy ribbons, the shear slip bands formed on the surface of the samples after yield deformation also can be detected as shown in Figure
80 5a. In the end of tensile deformation, The rupture for the nearly parallel shear slip bands are generated on the fracture surface as shown in Figure 5b. For the Ti75Zr11Si9Fe5 alloy ribbons, the fracture of the nearly parallel shear slip bands occurs along the

maximum stress plane during tensile test.

The protuberating characteristics along the shear bands are not visible on the sample surface, as shown in Figure 5a and 5b. Fracture surface of the Ti75Zr11Si9Fe5 alloy ribbons after tensile testing indicate that only insignificant homogenous deformation takes place before fracture. The enhancing mechanism by nano-Ti_5Si_3 particles does not occur for this alloy, because of no detectable Ti_5Si_3 phase formed in glassy Ti phase matrix. Most of the fracture surface has a textured structure, as shown in Figure 5a. Such a textured structure may lead to anisotropic properties of the ribbons. The direction parallel to the slip bands has a high tensile strength but lower shear strength and lower plasticity.

While Adding 3 at. % Mo, the ultimate tensile stress is enhanced to 2085 MPa for the Ti66Zr11Si15Fe5Mo3 alloy ribbons. The stress–stain curve reveals that $\sigma_{0.2}$ is about 1790 MPa, and about 4.87% plastic strain occurs before failure. Young's modulus is 94.3 GPa, which is close to the value of other non-bioTi-base BMGs [29-33]. Nearly all the Ti66Zr11Si15Fe5Mo3 alloy ribbons exhibits measurable plastic strain, and Young's modulus is close to that of conventional non-bioTi-base alloys.

The fast fracture of bulk amorphous after yielding is due to bulk amorphous own local shearing deformation softening mechanism that exists in the different amorphous systems during the deformation. Therefore, it is a bulk amorphous' mechanical characteristics in common. It is necessary to introduce a second phase in the glassy matrix to overcome the low plasticity of bulk amorphous structure [7]. Through the dispersed second phase to prevent deformation during amorphous local shear softening process, thus extending the deformation process of amorphous and improve ductility. As matter of fact, *in situ* Ti_5Si_3 nanoparticles coated β-Ti core-shell structure in glassy Ti matrix play a significant role in dispersion toughening, for the Ti66Zr11Si15Fe5Mo3 alloy ribbons.

We can observe and find the formation of slip band patterns on the surface of Ti66Zr11Si15Fe5Mo3 sample during the yield deformation using a SEM, as shown in Figure 5c. SEM image as shown in Figure 5b shows the micro-appearance of the shear band arrays with protuberance on the fracture surface of the specimen of Ti66Zr11Si15Fe5Mo3. The formation of protuberance on the fracture surface is attributed to 3 at. % Mo addition in this kind of Ti alloy.

Figure 5 reveals that the fracture goes along with the formation of veins along the shear-off direction. An overview of the fracture surface is shown in Figure 5c and 5d revealing that the slip band patterns originating from the shear band extend to the shear-off direction and the protuberating characteristics over the entire yield and fracture surface. This behaviour is very similar to that of single-phase BMGs [7, 9]. Figure 5d shows shear band arrays on the sample surface. Arrows in the magnified area indicate slip stopped by the particles containing Mo on the shear bands. Obviously, the shear bands already experience severe deformation during the yield deformation before fracture, as revealed by the formation and protuberance of multi-slip bands.

4. Conclusions

Amorphous Ti alloys are generally prepared by the design of components with the glass forming ability and rapid solidification process.

Accordingly, a number of studies on amorphization of Ti-based alloys have been carried out for the last two decades presumably because the amorphization is expected to cause remarkable increases in mechanical strength and corrosion resistance.

Despite the amorphous Ti alloy has high strength and other excellent performance, but its ductility is poor, therefore, how to improve the ductility of the amorphous alloy is an urgent problem.

In situ Ti_5Si_3/β-Ti nano-core-shell structure toughened and strengthed glassy Ti alloy matrix composites is obtained by the melt-spun rapid solidification for the Ti66Zr11Si15Fe5Mo3 alloy, which exhibits a very good combination of high strength and large ductility (over 4.8% plastic strain).

We found in that the stable phases after heating are Ti glassy matrix and nano-Ti_5Si_3 particles encircled by nano shell of β-Ti. For the Ti66Zr11Si15Fe5Mo3 ribbons, its high strength is attributed to both Mo solution strengthening and nano core-shell Ti_5Si_3/β-Ti toughening and dispersion strengthening, and the toughening contribution comes mainly from the nano core-shell Ti_5Si_3/β-Ti. The slip band patterns were formed on the surface of both melt-spun ribbons during the yield deformation, the slip band patterns originated from the shear band extend to the shear-off direction. For the Ti75Zr11Si9Fe5 alloy ribbons, the fracture of the nearly parallel shear slip bands occurs along the maximum stress plane during tensile test.

The tensile test results show that the amorphous Ti alloy matrix can be strengthened and toughened significantly by *in situ* Ti_5Si_3/β-Ti nano-core-shell structure.

Notes and references

a Address, No.8,Road No.1, Dingzigu, Hongqiao District, Tianjin, China. Fax: 22- 2656 4125; Tel: 22- 6020 4125; E-mail: hutcui@hebut.edu.cn

1   O.M. Ivasyshyn, A.V. Aleksandrov, Mater. Sci., 2008, **44**, 311.
2   M. Jahedi, S. Zahiri, S. Gulizia, B. Tiganis, C. Tang, D. Fraser, Mater. Sci. Forum. 2009, **505**, 618.
3   F.H. Froes, C. Suryanarayana, D. Eliezer, *ISIJ Int.* 1991, **31**, 1235.
4   G.Adam, D.L. Zhang, J. Liang, I. Macrae, Adv. Mater. Res. 2007, **29–30**, 147.
5   J.M. Capus, *Met. Pow. Rep.* 2005, **60**, 22.
6   A. Inoue, Acta Mater. 2000, **48,** 279.
7   A. Inoue, A. Takeuchi, Mater. Trans. 2002, **43**, 1892.
8   J. Zarzycki, Glasses and the Vitreous State 398–404 (Cambridge Univ. Press, Cambridge, 1991).
9   M.X. Xia, S.G. Zhang, C.L. Ma, and J.G. Li, Applied physics letters, 2006, **89**, 091917-098919.
10   A. Takeuchi, A. Inoue, Mater. Sci. Eng. A, 2001, **446**, 304.
11   T. Zhang, A. Inoue, Materials Science and Engineering A, 2001, **304-306**, 771.
12   Choi-Yim H., Johnson, W.L. Bulk metallic glass matrix composites. Appl. Phys. Lett. 71, 3808-3810 (1997).
13   C. Y. Cui, D.H.Ping, J. Alloy Compd. 2009, **471**, 248.
14   L.Q. Xing, Y.T. Shen, K.F. Kelton, Appl.Phys. Lett. 2002, **81**, 3371.
15   R.J. He, H.M.Wang, Mater. Sci. Eng. A. 2010, **527**, 1933.
16   J. Kim, S. Cho, S.Sures, A.S. Argon, Science, 2002, **295**, 654.

17 B. Clausen, S.Y. Lee, E.U. Üstündag, C.P. Kim, D.W. Brown, M.A.M. Bourke, Scripta Mater. 2006, **54**, 343.

18 F. Szuecs, C.P. Kim, W.L. Johnson, Acta Mater. 2001, **49**, 1507.

19 U. Kühn, J. Ecker, N. Mattern, L. Schultz, Appl. Phys. Lett. 2002, **80**, 2478.

20 S.L. Zhu, G.Q. Xie, F.X. Qin, X.M. Wang, Materials Science Forum, 2012, **750**, 36.

21 S.L. Zhu, X.M. Wang, F.X. Qin, et al., Intermetallics, 2008, **16**, 609.

22 E.H. Yin, M. Zhang, S.J. Pang, X.J. Zhao, T. Zhang, Journal of alloys and compounds, 2010, **504**, S10.

23 B.C. Lu, Y.L. Wang, J. Xu, Journal of alloys and compounds, 2009, **475**, 157.

24 M. Fukuhara, H. Yoshida, M. Sato, K. Sugawara, T. Takeuchi, I. Seki, T. Sueyoshi, Physica status solidi-rapid research letters, 2013, **7**, 477.

25 S.Abdi, M. S. Khoshkhoo, O.Shuleshova, et al. Intermetallics, 2014, 46, 156.

26 S. Pang, C.H. Shek, C.L. Ma, A. Inoue, T. Zhang, Mater. Sci. & Eng. A., 2007, **449**, 557.

27 G. He, J. Eckert, M. Hagiwara, Journal of applied physics, Vol. 2004, **95**, 1816.

28 W. Li, S. Shan, Q.H. Fang, Surface Engineering, 2012, **28**, 594.

29 D.V. Louzguine, A. Inoue, Scripta Mater. 2000, **43**, 371.

30 C. A. Schuh, A. C. Lund, Nature Mater. 2003, **2**, 449.

31 R.J. He, H.M. Wang, Mater. Sci. Eng. A. 2010, **527**, 1933. .

32 X.D.Wang, Q.Y. Shi, X. Wang, Z.L. Zhang, Mater. Sci. Eng. A. 2010, **527**, 1008.

33 S.-H. Kim, S. Y. Lee, S.-M. Yang, G.-R. Yi, NPG Asia Mat. 2011, **3**, 25.